# Synergistic Targeting of Cell Membrane, Cytoplasm, and Nucleus of Cancer Cells Using Rod-Shaped Nanoparticles

Sutapa Barua and Samir Mitragotri*

Department of Chemical Engineering, Center for Bioengineering, University of California, Santa Barbara, Santa Barbara, California 93106, United States

ABSTRACT Design of carriers for effective delivery and targeting of drugs to cellular and subcellular compartments is an unmet need in medicine. Here, we report pure drug nanoparticles comprising camptothecin (CPT), trastuzumab (TTZ), and doxorubicin (DOX) to enable cell-specific interactions, subcellular accumulation, and growth inhibition of breast cancer cells. CPT is formulated in the form of nanorods which are coated with TTZ. DOX is encapsulated in the TTZ corona around the CPT nanoparticle. Our results show that TTZ/DOX-coated CPT nanorods exhibit cell-specific internalization in BT-474 breast cancer cells, after which TTZ is recycled to the plasma membrane, leaving CPT nanorods in the perinuclear region and delivering DOX into the nucleus of the cells. The effects of CPT-TTZ-DOX nanoparticles on growth inhibition are synergistic (combination index = 0.17 ± 0.03) showing $10-10\,000$-fold lower inhibitory concentrations (IC_{50}) compared to those of individual drugs. The design of antibody-targeted pure drug nanoparticles offers a promising design strategy to facilitate intracellular delivery and therapeutic efficiency of anticancer drugs.
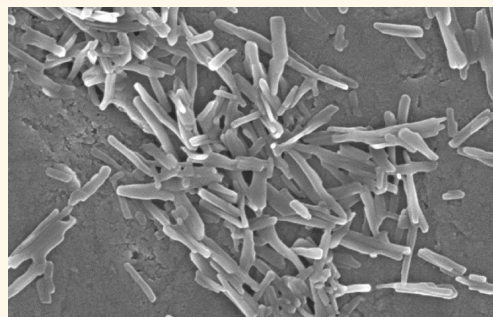
KEYWORDS: camptothecin · herceptin · doxorubicin · nanoparticle · shape · synergistic · morphology

F ormulating drugs to bind to desired cellular and subcellular targets is a necessary step in the design of anticancer therapies. Toward this goal, nanocarriers of polymers,[1] gold,[2] iron,[3] carbon nanotubes,[4] quantum dots,[5] micelles,[6] and liposomes,[7] among others, have been developed and have been targeted to various cells using antibodies,[1,2,8,9] aptamers,[10−13] and peptides.[7,14,15] Interactions of drug nanocarriers with the cell membrane and their intracellular localization depend on the nanocarrier's size, shape, and surface chemistry. The size of nanocarriers has been shown to impact the extent and the mechanism of cellular internalization.[16] Particle shape has been shown to impact the extent as well as specificity of internalization.[17−20] Following internalization, drug nanocarriers are transported progressively to the endosomes, recycling endosomes, acidic lysosomes, mitochondria, or nucleus, depending on the drug's physicochemical properties.[16,19,21,22] During the intracellular transport, it is often desirable to protect drugs

from the degradation in the acidic lysosomes. Drug nanocarriers with folate,[23,24] transferrin,[2] or other monoclonal antibodies[9] have been shown to release drugs in early endosomes, thereby minimizing potential drug loss due to acidification. These targeted drug nanocarriers have been shown to be more effective than free drugs both *in vitro* and *in vivo*.[24−26]

In this study, we explore subcellular distribution and therapeutic efficiencies of pure drug nanorods prepared using a combination of a hydrophobic anticancer drug camptothecin (CPT), a monoclonal antibody, trastuzumab (TTZ), and a water-soluble anticancer drug, doxorubicin (DOX). CPT is a topoisomerase I (topoI) enzyme inhibitor that targets the cleavable DNA-topoI complex (topoIcc).[27−29] CPT stacks between the DNA and topoIcc, prevents their dissociation, and induces replication/transcription-mediated DNA damage.[27,28] It selectively sensitizes cancer cells compared to normal cells by exhibiting S phase cytotoxicity and G2-M cell cycle arrest. However, the major

* Address correspondence to
samir@engineering.ucsb.edu.

limitations of CPT in clinical applications include its chemical instability in the lactone ring form, which gets converted to toxic carboxylate form at physiological pH, and inability to penetrate cell membrane and drug efflux by p-glycoproteins. TTZ is an FDA-approved humanized monoclonal therapeutic antibody for the treatment of breast, colon, and gastric cancers.[30−34] However, its individual treatment shows a low response of 12−34%.[31,33,35] Combination of TTZ with other anticancer drugs such as capecitabine, docetaxel, DOX, gemcitabine, paclitaxel, platines, vinorelbine, and other therapeutic antibodies (e.g., pertuzumab) has shown improved therapeutic effects.[35−39] DOX interferes with nucleic acid synthesis by intercalating between DNA base pairs in fast growing cancer cells and the DNA topoisomerase II (topoII) enzyme by inhibiting the relaxation of supercoiled DNA during transcription.[40] DOX is a first-line chemotherapeutic agent against many types of cancers including breast, lung, ovarian, and uterine cancers.[41] However, its severe cardiotoxicity and other side effects have limited its use with a maximum tolerated dose of 550 mg/m^2.[42] We sought to address limitations of CPT, TTZ, and DOX by using their combinations in a synergistic manner.

RESULTS

Synthesis and Characterization of CPT-TTZ-DOX Nanoparticles. Rod-shaped CPT nanoparticles were prepared using the solvent-diffusion method, and the surfaces of the nanoparticles were coated with TTZ by physical adsorption. DOX was incorporated into CPT-TTZ nanoparticles by coincubation. The SEM images of CPT nanorods, CPT-TTZ nanorods, and CPT-TTZ-DOX nanorods are shown in Figure 1. The dimensions of these rods are 509.5 ± 202.6 × 52.7 ± 18 nm, 511 ± 156.9 × 56.7 ± 14.7 nm, and 634.5 ± 146.9 × 100.8 ± 14.8 nm, respectively. The w/w ratio of CPT/TTZ and CPT/DOX are 6 ± 0.1 and 0.38 ± 0.07, respectively (Supporting Information (SI) Table I). CPT-TTZ and CPT-TTZ-DOX particles possessed slightly negative surface zeta-potentials (SI Table 1). CPT nanorods do not aggregate in PBS or even in medium, consistent with their strong negative zeta-potential (SI Table 1). The SEM images show appearance of aggregation due to drying of samples on the SEM stub.

Incubation of CPT nanorods in PBS for 72 h at physiological or low pH did not cause an appreciable change in size or shape (SI Figure 1). This is consistent with low solubility of CPT in water (negligible in water and ∼3 µg/mL in 0.1 M acetate buffer at pH 5[43,44]). Both TTZ and DOX were released from the CPT surface. Desorption of TTZ from CPT particles has been previously characterized;[20] only 12% TTZ desorbed after 2 h and 22% in 24 h when the particles were incubated with 10% fetal bovine serum (FBS) containing PBS buffer (pH 7.4) at 37 °C. The amount of DOX release from CPT-TTZ-DOX nanoparticles was investigated in the same media (SI Figure 2). About 25, 45, and 55% of the loaded DOX was released after 30 min, 1 h, and 2 h, respectively. This profile agrees with those reported previously.[45]

Intracellular Uptake of CPT-TTZ. We first investigated intracellular delivery of Alexa 594-conjugated CPT-TTZ in BT-474 cells using confocal microscopy. CPT, because of its inherent fluorescence property, was highly fluorescent in the blue region upon excitation using a 405 nm UV laser (for details see SI Text 1). After 2 h incubation, CPT-TTZ accumulated in the cytoplasm, showing high colocalization between Alexa 594-TTZ (red) and CPT nanorods (blue) inside the cells (Figure 2a and SI Figure 3). CPT nanorods without TTZ did not penetrate the cell membrane to a detectable extent (SI Figure 4a). To confirm that CPT-TTZ uptake occurs via specific interactions, cells were preincubated with excess of TTZ before exposure to CPT-TTZ. Indeed, no intracellular Alexa 594-TTZ or CPT signals were detected after blocking the receptor binding sites for TTZ (SI Figure 4b).

Upon internalization, Alexa 594-TTZ and CPT colocalized up until 2 h ($R = 0.73$, Pearson's correlation coefficient, $R_r = 0.7$) (Table 1 and SI Text 2). The extent of colocalization decreased over 24 h, indicating dissociation of TTZ from CPT over prolonged periods (Figure 2b and Table 1). It is likely that CPT-TTZ nanorod-containing early endosomes fuse to form sorting endosomes, where TTZ dissociates from CPT nanorods followed by recycling back to the plasma membrane. Indeed, experiments performed using Alexa 488-conjugated transferrin, a known endosomal recycling marker, indicated strong association of CPT-TTZ with sorting endosomes (Figure 3, Table 2, and SI Text 3).

TTZ recycling is also evident from red fluorescence of Alexa 594 at the plasma membrane (Figure 2b). A continuous, high concentration of red signals was detected along the cell membrane of BT-474 cells,
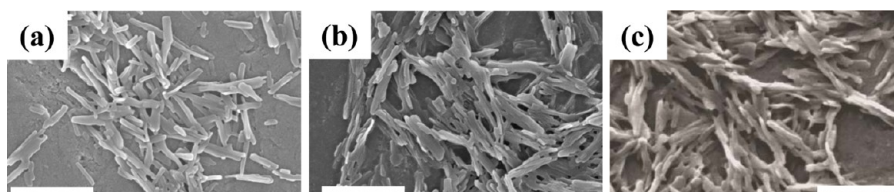

Figure 1. Scanning electron microscopy (SEM) showing the morphology and size of CPT, CPT-TTZ, and CPT-TTZ-DOX nanorods. Scale bar = 500 nm.
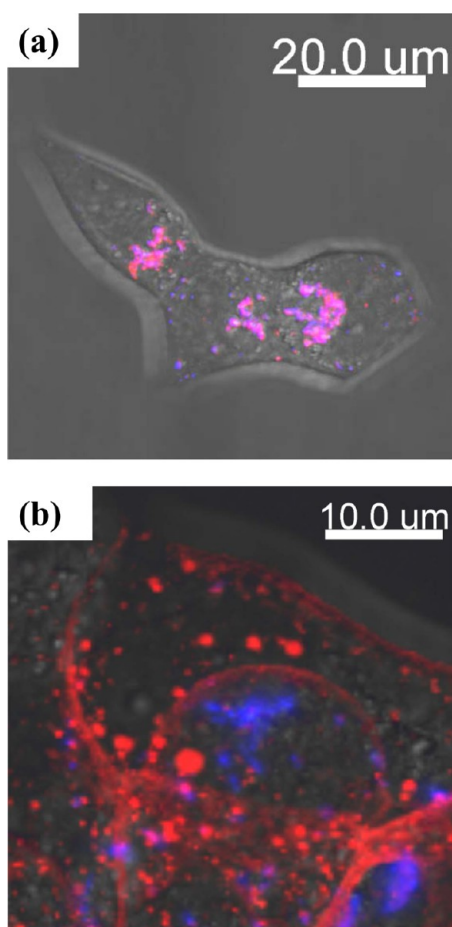
Figure 2. Intracellular localization of CPT (blue) and Alexa 594-conjugated TTZ (red) in BT-474 live cells after (a) 2 h and (b) 24 h incubation. BT-474 cells were treated with CPT-TTZ nanoparticles for 2 h, then (a) subsequently prepared for live cell imaging, or (b) incubated in fresh medium for 24 h at 37 °C and imaged in live cells. The blue, red, and DIC images are overlaid using Imaris. Magenta areas correspond to colocalization between CPT and TTZ.

TABLE 1. Quantitative Colocalization Analysis of the Confocal Microscopic Images of Alexa 594 Conjugated TTZ (Red) and CPT (Blue)[a]

incubation time (h)	Pearson's correlation coefficient, R_r	overlap coefficient, R	colocalization coefficients, m_1 and m_2
2	0.7 ± 0.15	0.73 ± 0.03	0.63 ± 0.18
			0.99 ± 0.02
24	0.2 ± 0.02	0.44 ± 0.15	0.58 ± 0.04
			0.62 ± 0.15

[a] The colocalization coefficients were calculated using ImageJ's intensity correlation analysis plugin and Imaris software. The Pearson's correlation coefficient, R_r, represents a correlation (positive, negative, or zero) between red (TTZ) and blue (CPT) signals. The overlap coefficient, R, demonstrates percentage colocalization between TTZ and CPT; m_1 and m_2 are colocalization coefficients of TTZ and CPT, respectively.

indicating the predominant localization of TTZ at the cell surface. In contrast, free TTZ (stained with Alexa 594) was not recycled back to the plasma membrane even after 24 h when the cells were coincubated with

CPT-DMSO and TTZ solution in PBS, simultaneously (SI Figure 4c). Free TTZ was internalized by the cells and remained inside the cells, indicating no comparable recycling. CPT-DMSO precipitated outside the cells due to insolubility in water and could not be internalized by the cells (SI Figure 4c). Taken together, these data suggest that the overall properties of CPT-TTZ, including size and shape, play a key role in determining the intracellular distribution of the drugs.

The average fluorescence intensity of Alexa 594-TTZ per cell in BT-474 cells did not change between 2 and 24 h (SI Figure 5), suggesting that only a small fraction of internalized TTZ is degraded and a majority is recycled back to the plasma membrane. To eliminate the possibility that Alexa 594 dye dissociated from TTZ conjugation and was retained at the cell surface, we incubated BT-474 cells with the equal concentration of Alexa 594-conjugated anti-human IgG-coated CPT nanorods and imaged cellular distribution of Alexa 594-IgG. Intracellular distribution of IgG was different than that observed for TTZ (SI Figure 6). IgG was localized in clusters inside the cell rather spreading in the cytoplasm and plasma membrane. In addition, the total fluorescence intensity of Alexa 594-IgG was 8.7 times lower than that measured for Alexa 594-TTZ. Overall, these results demonstrate that TTZ enhances CPT uptake and TTZ recycles back to the plasma membrane with no significant amount of degradation.

Subcellular Localization of CPT Nanorods. As an inhibitor of one of the nuclear enzymes, topoI, CPT is thought to localize inside the nucleus.[28,46] While that may be the case for soluble forms of CPT, nanorods of CPT were found to accumulate in the perinuclear region (Figure 4a,b). These observations were further validated with transmission electron microscopy. CPT was found in endosomes distributed from the plasma membrane close to the nucleus (Figure 4c and SI Figure 7a,b). No such particles were found in the cells treated with PBS (SI Figure 7c). Nuclear entry of CPT could not be seen in the TEM images. It is possible that small amounts of CPT dissolve within the cells and diffuse across the nuclear membrane into the nucleus.

DOX that was once associated with CPT-TTZ nanorods, on the other hand, readily entered the nuclei of the cells, while leaving CPT nanorods outside the nucleus (Figure 5). The precise time at which DOX dissociated from the nanorods is not clear. It is possible that DOX dissociated from the particles prior to their cellular entry and then diffused in the molecular form into the nucleus. Another possibility is that dissociation of DOX from nanorods occurred within the endosomes, followed by its diffusion into the nucleus. Free DOX, when incubated with a drug cocktail of CPT-DMSO and TTZ solution simultaneously, was also detected in the nuclei of the cells (SI Figure 4c). However, quantitative analysis showed that the average fluorescence intensity of DOX per cell (42.9 ± 5.1) in
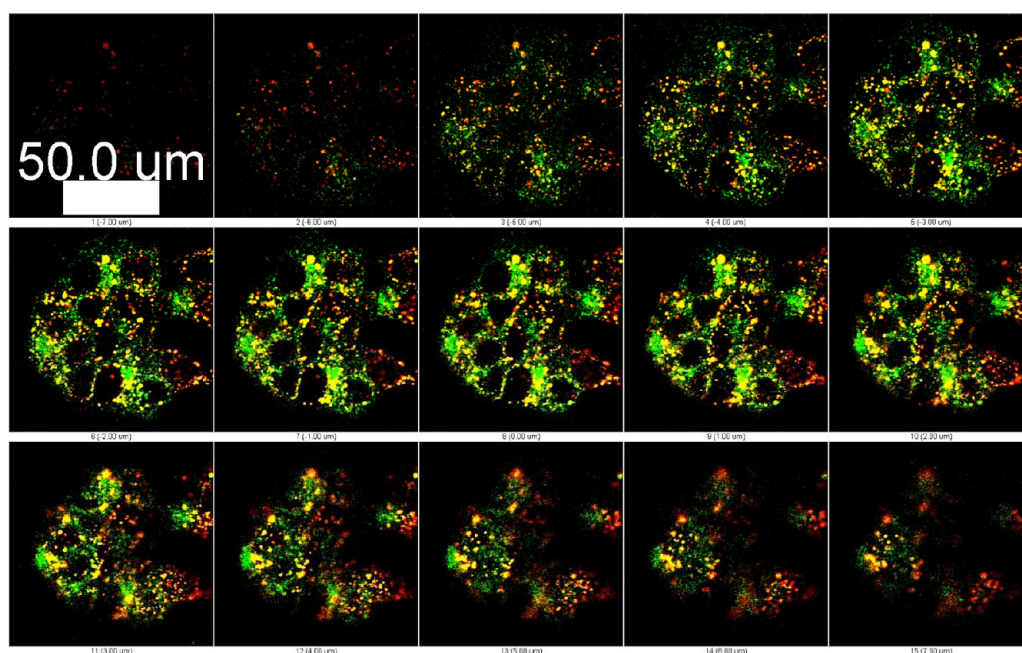
Figure 3. Intracellular colocalization of surface-bound Alexa 594 TTZ (red) with the recycling endosome marker, transferrin (green). CPT-Alexa 594-TTZ nanoparticles were incubated with BT-474 cells for 2 h at 37 °C and removed. Transferrin was added to the cells in fresh medium and incubated for an hour at 37 °C. Cells were washed using PBS and reincubated in fresh medium for confocal microscopy. The z-stacks at every 1 μm cell section are shown. Greater colocalization (yellow) occurs in the middle sections of the cells than the top or bottom sections.

TABLE 2. Colocalization Coefficients Were Calculated To Estimate the Colocaliztaion between TTZ (Red) with Recycling Endosomal Marker, Transferrin (Green), and CPT (Blue) with Transferrin (Green)

channels	Pearson's correlation coefficient, R_r	overlap coefficient, R	colocalization coefficients, m_1 and m_2
red/green (TTZ/transferrin)	0.44 ± 0.17	0.77 ± 0.13	0.72 ± 0.04
			0.84 ± 0.08
green/blue (transferrin/CPT)	0.13 ± 0.03	0.24 ± 0.11	0.52 ± 0.04
			0.3 ± 0.06

CPT-TTZ-DOX is almost 1.7 times higher than that of free DOX (25.1 ± 10) per cell, indicating higher accumulation of DOX inside the nucleus using CPT-TTZ-DOX. These results verify that the combination of CPT-TTZ-DOX nanoparticles complements subcellular distribution to attribute to better efficacy than free drugs.

***In Vitro* Cell Growth Inhibition by CPT-TTZ-DOX.** The effect of CPT-TTZ-DOX on *in vitro* grown inhibition of BT-474 cells was assessed. TTZ alone has an IC$_{50}$ of about 1000 μg/mL, above which the cell growth inhibition does not exhibit much dependence on concentration (SI Figure 8a). The IC$_{50}$ values for CPT and DOX are 1 and 4 μg/mL, respectively (SI Figure 8b,c). Theoretical potency (D_m) of CPT, TTZ, and DOX and the shape (m) of the dose effect curve of each drug are described in SI Text 4 and shown in SI Figure 8d−f. The combination CPT-TTZ-DOX yielded 45.5 ± 5.2% cell growth inhibition at concentrations of TTZ, CPT, and DOX of 0.02, 0.1, and 0.27 μg/mL, respectively (Figure 6), which are 10−50 000 times lower than those required to accomplish similar inhibition with individual drug treatments (SI Figure 8). Individual drug concentration at the same

value as that used in CPT-TTZ-DOX nanorods induced less than 20% growth inhibition (Figure 6); CPT-BSA-DOX particles induced only 16 ± 2.7% % inhibition, confirming the role of TTZ in the activity of CPT-TTZ-DOX. Simultaneous delivery of CPT-BSA nanoparticles, TTZ-coated polystyrene nanoparticles (SI Figure 9a and SI Text 5 for the preparation), and free DOX also showed lower growth suppression (20.2 ± 5.3%) than CPT-TTZ-DOX formulation, suggesting the CPT-TTZ nanorod assisted combination therapies. However, CPT-TTZ without DOX induced only 26.5 ± 8.9% inhibition, demonstrating that the addition of DOX to CPT-TTZ enhanced efficacy. The combination using the same concentrations of soluble CPT in DMSO or a water-soluble form of CPT (topotecan), TTZ solution, and free DOX inhibited cell growth by 26.3−30% (Figure 6), which is significantly less than that induced by CPT-TTZ-DOX single formulation. The synergy for CPT-TTZ-DOX is also specific for Her2 overexpressing cancer cells and is not seen in MDA-MB-231 cell line expressing lower or no Her2 (SI Figure 9b). The combination index (CI) based on the Chou−Talalay[47]
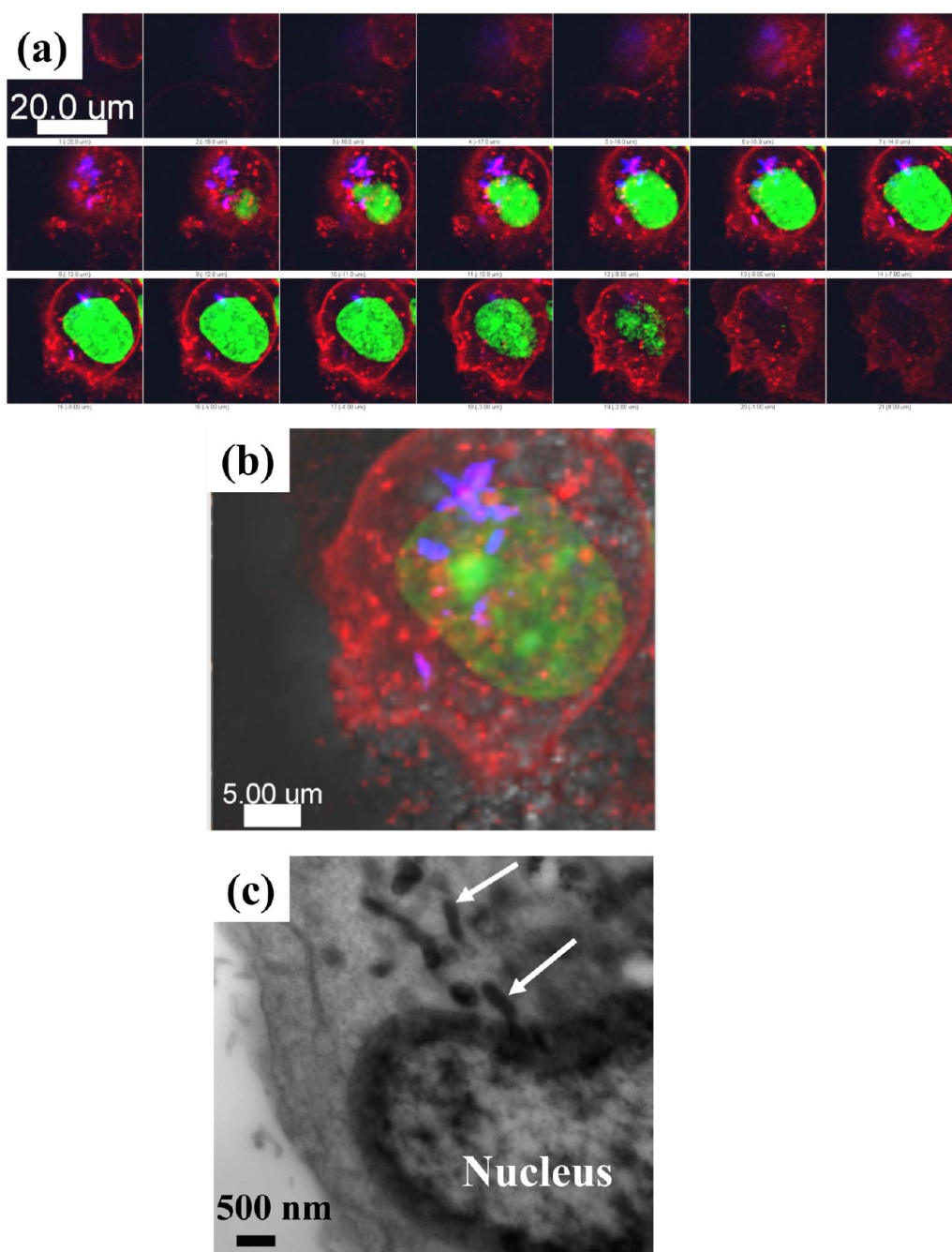
Figure 4. (a,b) Subcellular localization of CPT (blue) in live BT-474 breast cancer cells after 2 h CPT-Alexa 594-TTZ nanoparticle exposure followed by 24 h incubation in cell culture medium at 37 °C. The cell nuclei were stained with green SYTO13 (Molecular Probes). (a) Projections of 1 μm z-stacks showing the appearance of CPT nanoparticles close to the nucleus in the deeper sections of the cells. No CPT was found at the top or bottom cell sections. (b) Convergence of the z-stacks and DIC image. (c) TEM image of BT-474 cell section incubated for 24 h with an initial exposure to CPT-TTZ-DOX nanoparticles for 2 h. Arrows are showing localization of rod-shaped nanoparticles close to the nucleus.

equation was calculated as 0.17 ± 0.03, indicating highly synergistic actions of three drugs.

$$CI = \frac{0.02 \pm 0.004}{1000} + \frac{0.1 \pm 0.013}{1} + \frac{0.27 \pm 0.04}{4}$$

$$= 0.17 \pm 0.03 < 1; \text{synergy}$$

Effect on Cell Cycle. Mechanistically, TTZ, CPT, and DOX have been reported to arrest cells in the G0/G1 (resting phase), S (DNA synthesis), and G2/M (prior to cell division) phases, respectively.[46,48−50] Cell populations in each phase after exposure to CPT-TTZ-DOX were determined (Figure 7 and SI Figure 10). A high concentration (10 mg/mL) of TTZ solution was used as a positive control that arrested 85.6% cells in the G0/G1 phase (gray bars) compared to 41% in the absence of any drug (open bars). TTZ, adsorbed on polystyrene nanorods, was used as particulate form of the antibody.[20]
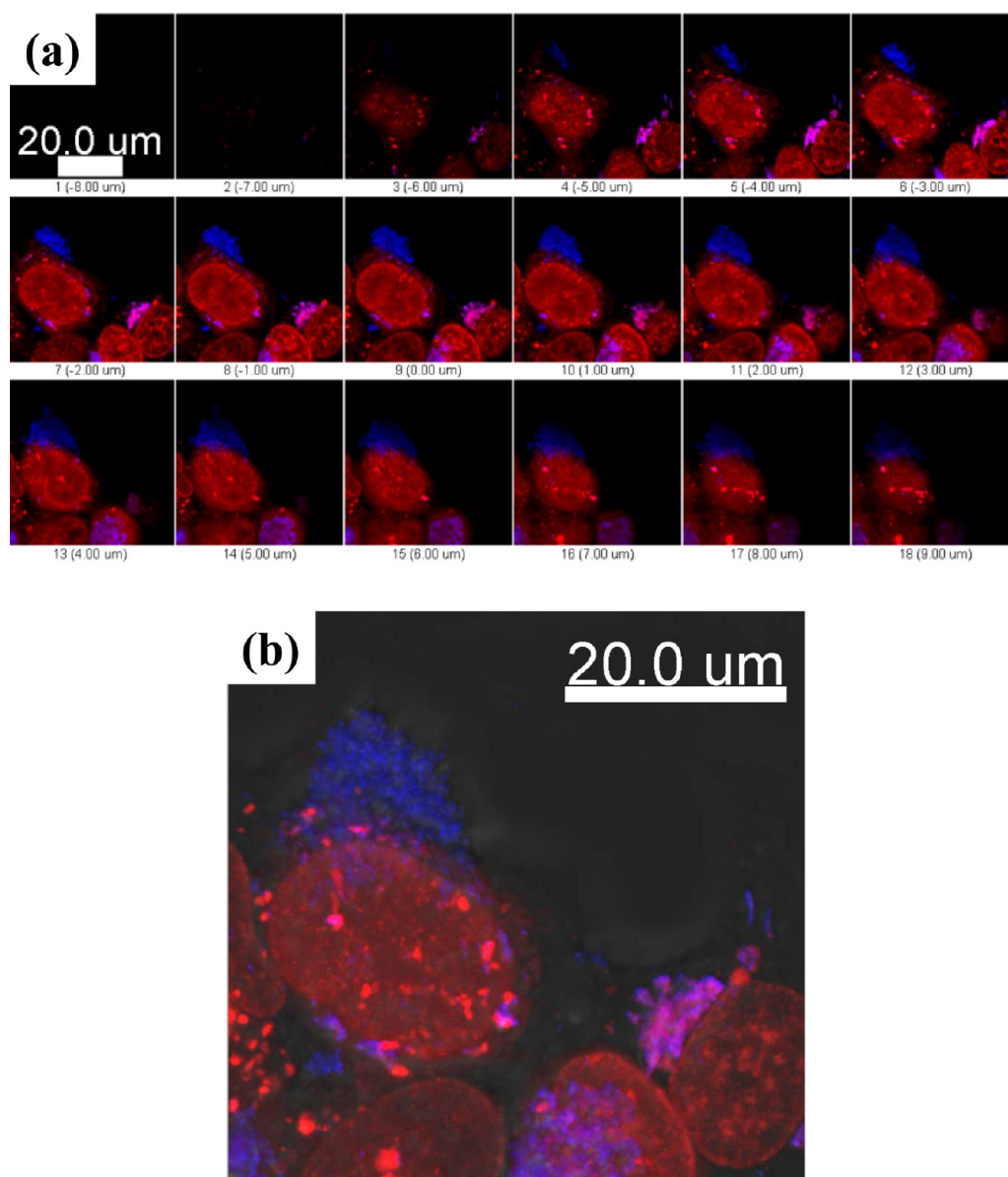
Figure 5. (a) Nuclear localization of red fluorescent DOX in BT-474 cells after 2 h incubation with CPT-TTZ-DOX particles. Cells were reincubated in cell culture medium at 37 °C for 24 h before confocal imaging. The blue signals show accumulation of CPT in the cytoplasm. (b) Overlay of the fluorescence images with DIC.

The physical properties of polystyrene nanorods were comparable to CPT nanorods (SI Figure 9a). TTZ nanorods, either polystyrene (hatched), CPT (two-way crossed), or CPT-DOX (black bars), arrested 55–60% cells in the G0/G1 phase, indicating that TTZ retains its function after adsorption to nanoparticle surfaces (Figure 7 and SI Figure 10). BSA-coated polystyrene rods did not exhibit elevated population in the G0/G1 phase compared to untreated control, confirming that neither polystyrene nor BSA affect cell cycle. CPT-TTZ nanorods arrested 24% cells in the S phase compared to <10% for controls, thus confirming preservation of CPT activity in the antibody-coated nanorod form. CPT-TTZ-DOX reduced the population in the S phase but increased the population in the G2/M phase compared to TTZ-polystyrene rods and

CPT-TTZ, indicating the effect elicited by DOX. However, the percentage of cells in the G2/M phase due to CPT-TTZ-DOX is lower than that of the untreated cells. Combined together, the effect of TTZ appears to be dominant in CPT-TTZ-DOX combination followed by DOX and CPT in that order.

DISCUSSION

Understanding the mechanisms of drug penetration into the cell and subcellular compartments has both pharmacodynamic and clinical applications. To elicit a therapeutic response, drug molecules must penetrate the cell surface and initiate their actions in cellular organelles. In this study, we show efficient intracellular delivery of a hydrophobic drug, CPT, and nuclear delivery
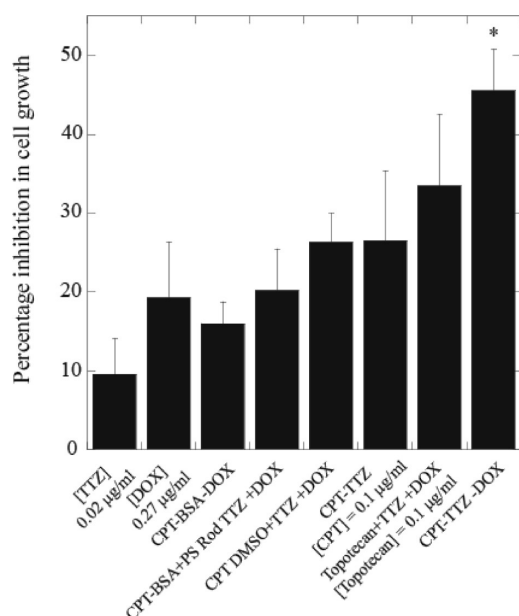
Figure 6. Effect of CPT-TTZ-DOX particles on cell growth inhibition of BT-474 cells. Data are shown as a percent inhibition of cell growth compared to PBS-treated control cells. The number of live cells was determined using calcein-AM (Molecular Probes). BT-474 cells were treated with 0.02 μg/mL TTZ solution, 0.27 μg/mL DOX solution, CPT-BSA-DOX, CPT-TTZ, and CPT-TTZ-DOX nanoparticles for 2 h followed by 72 h incubation in medium. Cells were also treated with the same concentrations of triple drug cocktails of CPT-BSA, TTZ-coated polystyrene, and free DOX; soluble CPT in DMSO, TTZ solution, and free DOX; and a soluble form of CPT (topotecan), TTZ solution, and free DOX. Columns represent mean values of three replicates. CPT-TTZ-DOX treatment is statistically significant ($p \leq 0.05$) compared with other treatments (SI Table 2) as indicated by the asterisk.
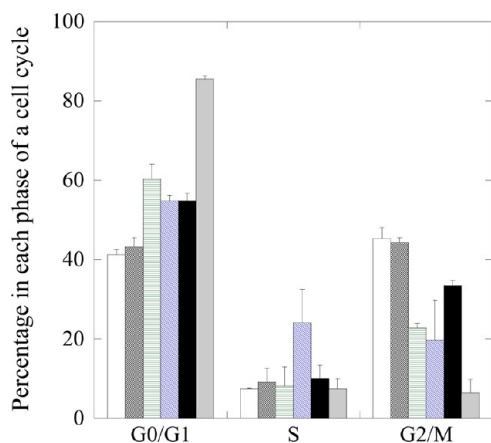

Figure 7. Effect on cell cycle in BT-474 cells. Cells were grown overnight in T25 flasks and incubated with PBS (open bars), BSA-coated polystyrene rod-shaped nanoparticles (dark gray), TTZ-coated polystyrene nanorods (green horizontal), TTZ-coated CPT nanorods (blue), CPT-TTZ-DOX (black bars), and TTZ solution (10 mg/mL) (light gray). After 2 h incubation, cells were incubated in fresh medium for 72 h, trypsinized, resuspended in HBSS, and stained with Vybrant DyeCycle Violet stain. At least 50 000 cells were analyzed by flow cytometry. The quantitative data of cell cycle distribution represents mean $\pm$ standard deviation.

of DOX using a pure drug nanoparticle construct, CPT-TTZ-DOX. TTZ induces the endocytosis of CPT. The results are consistent with the constitutive internalization and rapid recycling rate of the TTZ-Her2 receptor protein complex to the plasma membrane.[22] The endocytic sorting of TTZ-Her2 complexes in early and recycling endosomes (tubulovesicular compartment) has been reported at 16.6 and 70.5%, respectively, after 3 h incubation in SK-Br-3 cells.[22] TTZ-coated gold nanorods (60 × 13 nm) have been found to reside mostly in the early endosomes and then in lysosomes of SK-Br-3 cells after 6 h.[51] However, our results show CPT localization close to the nucleus after 24 h, but a majority of TTZ recycles back to the plasma membrane in the following mechanisms. The early endosomes carrying Tf and CPT-TTZ individually fuse and form a dynamic tubulovesicular endosomal compartment in which Tf, CPT, and TTZ are sorted out with the help of sorting nexin-4 (SNX4) protein.[22,52] The apo-Tf (Tf after releasing its iron content), TTZ, and their respective receptors are sorted out in the tubular compartments of the tubulovesicular endosome, pinched off from the vesicular compartment, and recycled back to the plasma membrane. CPT nanorods remain in the vesicular compartments of the endosome, are transported deeper in the cytoplasm, and matured to late endosomes.

Free TTZ was not recycled but instead was retained in endosomes, demonstrating the significance of endosomal sorting in the presence of CPT nanorods. The precise reason of TTZ recycling to the plasma membrane in case of CPT-TTZ, but not for free TTZ, is unknown; however, two reasons are possible. TTZ, when delivered in the soluble form, is likely released from Her2 receptors in the endosomes, thus preventing its recycling. On the other hand, it is possible that TTZ attached to CPT cannot be released from Her2 due to conformational changes in TTZ by hydrophobic interactions between CPT and TTZ, thus allowing its recycling. Another possibility is that free TTZ and CPT-TTZ arrest cell cycles in different stages, thus impacting the extent of TTZ recycling. Free TTZ arrests cells in the G0/G1 which is a rather quiescent phase where endosome recycling to the cell surface may be inhibited or slowed. In contrast, CPT-TTZ arrests cells in S phase where cells are more active. In addition to the TTZ-mediated endocytosis and cellular localization, the shape of CPT nanorods may also contribute to the enhanced uptake and intracellular sorting. Multivalent interactions between the rod-shaped CPT-TTZ nanoparticles and Her2 receptor proteins likely increase the binding affinity of the particles to the cell surface and eventually enhance intracellular delivery.[8,20,53] Theoretical models as well as *in vivo* biodistribution studies have suggested the benefits of using elongated particles for enhanced targeting ability and receptor-mediated cellular uptake.[18,54−56]

Previous studies in the literature have reported that size and shape impact intracellular uptake[18,57−59] and distribution of particles.[56,60] Intracellular trafficking of nonspherical particles conjugated with targeting ligands have different trafficking pathways compared to that of spherical particles.[56,58] Rod-shaped nanoparticles are reported to target the nucleus, while hexagonal sheet-like nanoparticles are retained in the cytoplasm.[61] This shape-dependent intracellular transport behavior is important to deliver drugs to the cytoplasm to protect them from lysosomal degradation. In a separate study, Kolhar *et al.* showed that cytoplasmic transport and accumulation of particles at the perinuclear region depend on their size and shape.[60] While the present study did not explore the effects of size and shape, it is possible that similar intracellular distribution of CPT, TTZ, and DOX may be observed using other nanoparticle size and shapes.

The solution form of CPT is expected to enter the nucleus and exhibit its activity as a nuclear topoI enzyme inhibitor.[28] In the nanorod form, however, a majority of CPT was found to reside outside the nucleus, most likely within the late endosomes. Two water-soluble CPT analogues, topotecan and gimatecan, are reported to localize in the mitochondria and endoplasmic reticulum and lysosomes, respectively, instead of the nucleus in HT-29 colon cancer cells.[62] Localization of CPT in the acidic lysosomes can be beneficial for enhancing the stability of the lactone ring of CPT in acidic pH[46] and the intracellular release of the drug within the cell. Some CPT could have entered the nucleus but not be detected within the detection limit of the confocal microscopy and TEM.

DOX entered the nucleus most possibly *via* the passive diffusion through the nuclear pore complexes of the nuclear membrane.[63] Several different approaches have been taken to promote nuclear delivery of DOX using nuclear localization signal (NLS)-conjugated poly(D,L-lactide-*co*-glycolide) (PLGA) nanoparticles,[64] NLS-conjugated glycol chitosan,[65] PEGylated liposomes,[7] micelles,[66] and polymers.[67] However, many of these approaches suffer from DOX protonation in the acidic pH.[68] CPT-TTZ-DOX nanoparticles led to a substantial accumulation of DOX inside the nucleus without significant detectable amounts of DOX in the cytoplasm, suggesting negligible DOX protonation. In addition, DOX binding to DNA has been reported to quench its fluorescence intensity, while DOX fluorescence intensity is enhanced when residing in the cytoplasm.[69] In our study, we found most of the DOX entered the nucleus of the cells which might cause lower DOX fluorescence intensity upon binding to DNA. Although the half-life of DOX release from the particles is ~2 h under physiological conditions, this time is significantly longer than the blood circulation half-life (5−10 min) of free DOX.[70] Upon *in vivo* administration, CPT-TTZ-DOX is expected to reach the tumor site within 30 min after administration, still carrying sufficient levels of DOX, and release the drug at the tumor site. Detailed pharmacokinetics and biodistribution studies are necessary to further assess this possibility.

The cell growth inhibition using CPT-TTZ-DOX was attributed to the cell cycle arrest showing a higher proportion of cells in the G0/G1, S, and G2/M phases than the respective controls. TTZ is known to induce cell cycle arrest in the G1 phase with a reduction of cell proliferation and induction of apoptosis.[48] CPT is an S-phase-specific DNA-topoI complex intercalator,[49] and DOX tends to arrest cells in the G2/M cell cycle.[50,71] The cell cycle data reported here show that individual components of CPT-TTZ-DOX nanoparticles retain their activity in the nanoparticulate form. *In vivo* investigations are necessary to confirm therapeutic benefits of this combination.

CPT itself has not been used for cancer therapy due to its insolubility in the aqueous phase. Hydrophobic CPT also shows limited interactions with cell membrane and diffusion inside the cytoplasm (SI Figure 4c). However, rod-shaped CPT nanorods, when coated by TTZ, exhibit significant intracellular uptake (Figure 2 *vs* SI Figure 4c). *In vitro* tests in BT-474 cells showed that CPT-TTZ-DOX can act synergistically at respective doses of 0.1, 0.02, and 0.27 μg/mL (or same numbers in mg/kg assuming the same concentration is to be achieved *in vivo*). CPT concentrations between 0.5 and 4.0 mg/kg have been reported to increase the lifetime of mice beating L1210 leukemia tumors.[72] TTZ doses up to 20 mg/kg have been used to disrupt Her2−Her3 association in BT-474-M1 tumor xenografts in mice.[73] Free DOX doses of 9 and 16 mg/kg have been used to study pharmacokinetics of the drug in mammary carcinoma (4T1) implanted mice.[74] The doses used in this *in vitro* study are significantly lower than those reported in the literature for *in vivo* studies.

The size of CPT nanorods can be further reduced to facilitate its *in vivo* use. Specifically, the length of CPT nanorods was reduced from 509.5 ± 202.6 × 52.7 ± 18 nm to ~290 ± 88 × 47.4 ± 19.1 nm by modifying the synthesis procedure (SI Figure 11 and SI Text 6). These newer generation CPT nanorods can be functionalized with TTZ using the same method as those used for longer nanorods. Nanoparticles with dimensions of 300 nm have been used for *in vivo* studies without causing any toxicity and aggregation problems.[75−77] This size is within the cutoff size of permeation across the vascular wall. Literature studies have shown that doxorubicin-loaded polymeric spheres (diameter = 300 nm) exhibit high accumulation at the tumor site after 1−3 days of intravenous injection.[77] Liposomes between 100 and 400 nm have also been reported to penetrate tumors in mice xenografts.[78] We have recently showed that rod-shaped nanoparticles of ~500 nm bind to lung and brain endothelial cells of mice better than spheres when coated with antibodies.[79]

Therefore, it can be anticipated that the CPT-TTZ-DOX holds significant promise for *in vivo* efficacy, although we agree that direct *in vivo* tests are necessary to confirm the efficacy.

CONCLUSION

In summary, we have formulated rod-shaped drug nanoparticles using three anticancer drugs to combine active targeting of cancer cells with improved therapeutic activity. The distinctive intracellular distribution of the drugs makes them suitable for multiple cytoplasmic targeting as well as synergistic efficacy even at very low drug concentrations. The *in vitro* tests offer detailed insights into the mechanisms of synergy. We expect that such *in vitro* studies will contribute to bridging the gap between *in vitro* design/characterization and *in vivo* therapeutic evaluations.

METHODS

Preparation of Camptothecin (CPT)-Trastuzumab (TTZ)-Doxorubicin (DOX) Nanoparticles. First, we prepared CPT nanorods using a solvent diffusion method and adsorbed TTZ and DOX on the surfaces of CPT nanorods. Briefly, 1 mL of 1 mg/mL CPT (Sigma-Aldrich) DMSO solution was injected into 50 mL of 1% polyvinyl alcohol (PVA; 13−23k; Sigma) water mixture using a syringe pump (kd Scientific Inc.). The mixture was stirred under 300 rpm at room temperature (22 °C). CPT nanorods formed at the boundary where DMSO diffused slowly into water. The nanorods were washed using milliQ water and centrifuged three times at 11 000 rcf for 1 h. The concentrations of CPT nanorods were measured by reading absorbance at 366 nm using a spectrophotometer (Tecan Saffire) and a CPT calibration curve.

TTZ (Gennentech) was conjugated with Alexa Fluor 594 dye using a protein labeling kit (Invitrogen). The moles of Alexa 594 dye per mole of TTZ protein was calculated to be 4.7 ± 0.09, which is in the acceptable range (2−6 mols) according to the vendor's protocol (Invitrogen). A 100 μL labeled or unlabeled TTZ solution (1 mg/mL) was added to 1 mL of 1 mg/mL CPT nanorods and incubated overnight at 4 °C. TTZ adsorbed CPT nanorods were purified by a 3-fold centrifugation and redispersion in phosphate buffer saline (PBS) buffer containing 0.1% BSA and 0.01% sodium azide. The supernatants collected during the centrifugation were analyzed using micro-BCA assay kit (Pierce) to measure the unbound TTZ. TTZ adsorption efficiency was calculated as the difference between the initial amount and the unbound antibody per milligram of CPT nanorods. Bovine serum albumin (Sigma) and Alexa 594-conjugated anti-human IgG (Molecular Probes) were adsorbed on CPT nanorods as controls.

Finally, DOX (1000 μg; Sigma) solution was added to 500 μg of CPT containing CPT-TTZ nanorods and incubated overnight at 4 °C in a rotator. The mixture was centrifuged three times at 1000 rcf for 10 min, where the supernatants were collected to measure the unbound DOX and CPT. A DOX standard calibration curve was plotted using standard concentrations of DOX dissolved in water. Fluorescence intensity of the DOX standards and supernatants were measured using an excitation/emission of 471 ± 9 nm/556 ± 25 nm. The amount of encapsulated DOX was calculated by subtracting the amount of DOX in the supernatants from the initial amount of DOX used.

Morphology of CPT nanorods, CPT-TTZ, and CPT-TTZ-DOX was visualized using a scanning electron microscope (SEM). The surface charges of the nanoparticles suspended in PBS were measured as zeta-potential using a Nanoseries Zetasizer (Malvern).

DOX Release from CPT-TTZ-DOX Nanoparticles. Freshly prepared nanoparticles were resuspended in 1 mL of 10% fetal bovine serum (FBS) containing phosphate buffer saline (PBS) at pH 7.4 and incubated at 37 °C. Nanoparticles were centrifuged to collect the supernatants, resuspended in 10% FBS-PBS, and further incubated. The release of DOX was measured at 0, 0.5, 1, 2, and 24 h by fluorescence spectrophotometry (ex/em = 471 ± 9 nm/556 ± 25 nm). The percentage of DOX release was calculated as $100 \times ((F_t - F_i)/(F_{total} - F_i))$, where F_t, F_i, and F_{total} are the fluorescence intensities at any time t, initial DOX, and total DOX solution.

Intracellular Localization of CPT-TTZ and CPT-TTZ-DOX. Intracellular uptake of CPT-TTZ was studied in BT-474 breast cancer cells (ATCC) by confocal microscope analysis. Her2 overexpressing

BT-474 cells were cultured in ATCC Hybricare medium was supplemented with 10% FBS at 37 °C and 5% CO_2 in a humidified incubator. Cells were seeded in an 8-well chambered coverglass (Lab-Tek II) at a density of 10 000 cells in 200 μL medium. After overnight growth, cells were incubated with CPT-Alexa 594-conjugated TTZ, CPT-BSA, CPT-Alexa 594 IgG, and CPT nanorods alone where CPT, TTZ, BSA, and IgG concentrations were 300, 50, 36, and 50 μg/mL, respectively. In the case of CPT-TTZ-DOX nanoparticle incubation, the concentrations were 100, 16.7, and 260 μg/mL, respectively. To exclude the possibility of nonspecific cellular interactions by TTZ-coated nanoparticles, cells were preincubated with 100 μg/mL TTZ for 30 min and then treated with Alexa 594-CPT-TTZ particles. To verify the dependence of intracellular distribution of three drugs on nanoparticle geometry, cells were incubated with a drug cocktail of soluble CPT (solubilized in DMSO), TTZ, and DOX solution. Soluble CPT and Alexa 594-TTZ were used to interpret the localization of free TTZ. The drugs were added at the same concentrations as they were in the nanoparticles with every 15 min intervals by incubating the cells at 37 °C. After 2 h of total incubation at 37 °C, cells were washed three times using PBS. For recycling endosome staining, cells were incubated further for 1 h with 10 μg/mL Alexa 488-conjugated transferrin (Molecular Probes) and washed prior to imaging. Transferrin was added later to avoid its potential association with CPT-TTZ nanorods outside the cells (in the medium) which could confound the interpretation. To image the intracellular localization of CPT-TTZ and CPT-TTZ-DOX after 24 h, cells were washed after 2 h of particle exposure and reincubated in fresh medium. To stain the cell nuclei, cells were incubated with 1 μM green fluorescent nuclear stain, SYTO13 (Molecular Probes), for 1 h before washing. Imaging was performed within 1 μm inner sections of cells by sequential scanning using an Olympus confocal microscope (Fluoview 1000) equipped with a 60× silicone oil immersion objective. Fast sequential line scanning was carried out using acousto-optic tunable filters (AOTF) to avoid any crosstalk between image channels. AOTF rapidly turns on and off different laser lines in a few milliseconds that excites only one fluorophore at a time eliminating any crosstalk between image channels. In addition, control images were taken individually at the very beginning of the experiments to set up the excitation/emission settings. CPT, Alexa 488, SYTO 13, DOX, and Alexa 594 were excited with 405 diode, 488 argon, 488 argon, 488 argon, and 559 diode line lasers, respectively, and the emissions were collected at 461 ± 20, 520 ± 25, 510 ± 10, 575 ± 25, and 618 ± 50 nm wavelengths, respectively. The z-stacks of fluorescence images were merged and analyzed using Imaris (Bitplane) software. Fluorescence intensities of Alexa 594 and DOX per cell were analyzed for at least 10 cells.

Quantitative Colocalization Analysis. Colocalization analysis was done using Imaris, ImageJ 1.37a software (National Institute of Health; http://rsb.info.nih.gov/ij/) and its plugin, intensity correlation analysis. The RGB color images were converted into 8-bit colors using ImageJ. The 8-bit red and green channels for three independent samples were used to calculate the Pearson's correlation coefficient (R_r), overlap coefficient (R), and colocalization coefficients, m, for each channel. R_r measures if there is any correlation between two signal intensity in the range between −1 and 1, where −1, 0, and 1 indicate inverse, none,

and positive correlations between channels. *R* indicates the percent overlap of selected channels. Coefficient *m* describes the contribution of each pixel during colocalization. The percent of colocalizaton was calculated from these three coefficients.

Transmission Electron Microscopy (TEM). BT-474 cells were incubated with 300 μg/mL CPT-TTZ-DOX nanoparticles for 2 h followed by fresh cell culture medium for 24 h. Cells were postfixed using 2% glutaraldehyde solution in 0.1 M cacodylate buffer, stained using 1% osmium tetraoxide, dehydrated in graded ethanol series, infiltrated with propylene oxide/Spurr resin mixture, and embedded in Spurr resin. The embedded cells were cut into 90 nm ultrathin sections using an ultramicrotome and a glass knife. Three to four sections were mounted on 200 mesh copper grids, stained with uranyl acetate and lead citrate, and imaged in a JEOL 123 transmission electron moicroscope operated at 80 kV.

In Vitro Cytotoxicity of CPT-TTZ-DOX. *In vitro* activity of CPT-TTZ-DOX in BT-474 cells and Her2-negative MDA-MB-231 cells was analyzed using calcein AM of the live-dead assay kit (Invitrogen). BT-474 and MDA-MB-231 cells were seeded in 96-well plates at a density of 10 000 cells in 200 μL Hybricare medium (ATCC) and DMEM (ATCC), respectively, in 96-well plates, allowed to attach overnight, and treated with CPT-TTZ-DOX particles for 2 h with final doses of CPT, TTZ, and DOX as 0.1, 0.02, and 0.27 μg/mL, respectively. The following controls were used in BT-474 cells: PBS, TTZ (0.02 μg/mL) alone, DOX (0.27 μg/mL) alone, CPT-TTZ particles (0.1 and 0.02 μg/mL of CPT and TTZ, respectively), and CPT-BSA-DOX particles (0.1, 0.012, and 0.27 μg/mL of CPT, BSA, and DOX, respectively). To test if nanoparticle geometry influences the drug activity, BT-474 cells were incubated with the following controls by adding the drugs simultaneously at 15 min intervals: (i) soluble CPT in DMSO, TTZ solution, and free DOX; (ii) a soluble form of CPT (topotecan), TTZ solution, and free DOX; and (iii) CPT-BSA, TTZ-coated PS nanorods, and free DOX. Cells were incubated for the indicated time interval before adding each drug. After 2 h total incubation, medium was replaced with fresh medium, and the cells were further incubated for 72 h. Live cells were then measured using the live-dead assay kit (Invitrogen) and analyzed using a plate reader (Tecan Saffire). For quantification of the number of live cells, the medium was removed, and calcein AM (1 μM) in PBS was added to the cells and incubated at room temperature for 30 min. Fluorescence intensities of calcein AM (ex/em 495/530 $\pm$ 25 nm) was measured using the plate reader. Fluorescence backgrounds of PBS were subtracted from each well. Assays were performed at least in triplicate in three independent experiments. The results are expressed as percentage inhibition in cell growth relative to growth of PBS-treated control cells. Similarly, individual dose response curves of TTZ, CPT, and DOX were also performed to determine inhibitory drug concentrations (IC$_{50}$) to stop 50% cell growth. From the resulting curves of individual drug treatment and CPT-TTZ-DOX effects, the combination index (CI) for CPT-TTZ-DOX was calculated using the Chou-Talalay method:[47]

$$CI = \frac{(IC_{50} \text{ of TTZ in CPT} - TTZ - Dox)}{IC_{50} \text{ of TTZ solution}}$$
$$+ \frac{(IC_{50} \text{ of CPT in CPT} - TTZ - Dox)}{IC_{50} \text{ of CPT}}$$
$$+ \frac{(IC_{50} \text{ of Dox in CPT} - TTZ - Dox)}{IC_{50} \text{ of Dox}} \quad (1)$$

In this analysis, synergy is defined when CI < 1. Two-tailed, type 3 (samples with different variances) statistical tests were used to determine if the effect due to CPT-TTZ-DOX was significantly different from that of other data sets (*e.g.*, CPT-TTZ, CPT-BSA-DOX, *etc.*).

Cell Cycle Analysis. To determine the growth arrest induced by CPT-TTZ-DOX particles, we performed the DNA counts in BT-474 cells after exposure to polystyrene nanorods TTZ, CPT, and CPT-TTZ-DOX. Subconfluent monolayers of BT-474 cells (100 000) were grown in T-25 flasks in 5 mL medium. Cells were incubated with TTZ-coated polystyrene rods (100 μg/mL), CPT nanorods (10 μg/mL), CPT(10 μg/mL)-DOX (2.7 μg/mL) particles, PBS, and a high concentration (10 mg/mL) of TTZ solution

(a positive control) for 2 h. TTZ concentrations on polystyrene particles and CPT were 12.5 and 0.2 μg/mL, respectively. BSA-coated polystyrene rod was used as the negative control. The cells were then incubated in fresh medium for 72 h, trypsinized, and resuspended in 500 μL Hanks' balanced salt solution (HBSS). A DNA binding fluorescent dye and cell-permeant stain, Vybrant DyeCycle Violet, were added to the cell suspension at a concentration of 1 μM and incubated at 37 °C for 30 min by wrapping aluminum foils around the sample tubes. The cells were then analyzed on a BD FACSAria flow cytometer (BD Biosciences) using a UV light source. A minimum of 50 000 cells were analyzed for each sample in duplicate in two independent experiments.

REFERENCES AND NOTES

1. Sun, B.; Ranganathan, B.; Feng, S.-S. Multifunctional Poly(D,L-lactide-*co*-glycolide)/Montmorillonite (PLGA/MMT) Nanoparticles Decorated by Trastuzumab for Targeted Chemotherapy of Breast Cancer. *Biomaterials* **2008**, *29*, 475–486.
2. Choi, C. H. J.; Alabi, C. A.; Webster, P.; Davis, M. E. Mechanism of Active Targeting in Solid Tumors with Transferrin-Containing Gold Nanoparticles. *Proc. Natl. Acad. Sci. U. S. A.* **2010**, *107*, 1235–1240.
3. Mi, Y.; Liu, X.; Zhao, J.; Ding, J.; Feng, S. S. Multimodality Treatment of Cancer with Herceptin Conjugated, Thermomagnetic Iron Oxides and Docetaxel Loaded Nanoparticles of Biodegradable Polymers. *Biomaterials* **2012**, *33*, 7519–7529.
4. Fabbro, C.; Ali-Boucetta, H.; Ros, T. D.; Kostarelos, K.; Bianco, A.; Prato, M. Targeting Carbon Nanotubes against Cancer. *Chem. Commun.* **2012**, *48*, 3911–3926.
5. Gao, X.; Cui, Y.; Levenson, R. M.; Chung, L. W. K.; Nie, S. *In Vivo* Cancer Targeting and Imaging with Semiconductor Quantum Dots. *Nat. Biotechnol.* **2004**, *22*, 969–976.
6. Koo, O. M.; Rubinstein, I.; Onyuksel, H. Camptothecin in Sterically Stabilized Phospholipid Micelles: A Novel Nanomedicine. *Nanomedicine* **2005**, *1*, 77–84.
7. Wang, Z.; Yu, Y.; Dai, W.; Lu, J.; Cui, J.; Wu, H.; Yuan, L.; Zhang, H.; Wang, X.; Wang, J.; *et al*. The Use of a Tumor Metastasis Targeting Peptide To Deliver Doxorubicin-Containing Liposomes to Highly Metastatic Cancer. *Biomaterials* **2012**, *33*, 8451–8460.
8. Tsai, C.-P.; Chen, C.-Y.; Hung, Y.; Chang, F.-H.; Mou, C.-Y. Monoclonal Antibody-Functionalized Mesoporous Silica Nanoparticles (MSN) for Selective Targeting Breast Cancer Cells. *J. Mater. Chem.* **2009**, *19*, 5737–5743.
9. Kocbek, P.; Obermajer, N.; Cegnar, M.; Kos, J.; Kristl, J. Targeting Cancer Cells Using PLGA Nanoparticles Surface Modified with Monoclonal Antibody. *J. Controlled Release* **2007**, *120*, 18–26.
10. Farokhzad, O. C.; Cheng, J.; Teply, B. A.; Sherifi, I.; Jon, S.; Kantoff, P. W.; Richie, J. P.; Langer, R. Targeted Nanoparticle–Aptamer Bioconjugates for Cancer Chemotherapy *in Vivo*. *Proc. Natl. Acad. Sci. U.S.A.* **2006**, *103*, 6315–6320.

11. Bagalkot, V.; Zhang, L.; Levy-Nissenbaum, E.; Jon, S.; Kantoff, P. W.; Langer, R.; Farokhzad, O. C. Quantum Dot–Aptamer Conjugates for Synchronous Cancer Imaging, Therapy, and Sensing of Drug Delivery Based on Bi-Fluorescence Resonance Energy Transfer. *Nano Lett.* **2007**, *7*, 3065–3070.

12. Xiao, Z.; Levy-Nissenbaum, E.; Alexis, F.; Lupták, A.; Teply, B. A.; Chan, J. M.; Shi, J.; Digga, E.; Cheng, J.; Langer, R.; *et al.* Engineering of Targeted Nanoparticles for Cancer Therapy Using Internalizing Aptamers Isolated by Cell-Uptake Selection. *ACS Nano* **2012**, *6*, 696–704.

13. Dam, D. H. M.; Lee, J. H.; Sisco, P. N.; Co, D. T.; Zhang, M.; Wasielewski, M. R.; Odom, T. W. Direct Observation of Nanoparticle–Cancer Cell Nucleus Interactions. *ACS Nano* **2012**, *6*, 3318–3326.

14. Sugahara, K. N.; Teesalu, T.; Karmali, P. P.; Kotamraju, V. R.; Agemy, L.; Greenwald, D. R.; Ruoslahti, E. Coadministration of a Tumor-Penetrating Peptide Enhances the Efficacy of Cancer Drugs. *Science* **2010**, *328*, 1031–1035.

15. Howarth, M.; Takao, K.; Hayashi, Y.; Ting, A. Y. Targeting Quantum Dots to Surface Proteins in Living Cells with Biotin Ligase. *Proc. Natl. Acad. Sci. U.S.A.* **2005**, *102*, 7583–7588.

16. Zhang, S.; Li, J.; Lykotrafitis, G.; Bao, G.; Suresh, S. Size-Dependent Endocytosis of Nanoparticles. *Adv. Biomater.* **2009**, *21*, 419–424.

17. Yoo, J.-W.; Doshi, N.; Mitragotri, S. Endocytosis and Intracellular Distribution of PLGA Particles in Endothelial Cells: Effect of Particle Geometry. *Macromol. Rapid Commun.* **2010**, *31*, 142–148.

18. Gratton, S. E.; Ropp, P. A.; Pohlhaus, P. D.; Luft, J. C.; Madden, V. J.; Napier, M. E.; DeSimone, J. M. The Effect of Particle Design on Cellular Internalization Pathways. *Proc. Natl. Acad. Sci. U.S.A.* **2008**, *105*, 11613–11618.

19. Vácha, R.; Martinez-Veracoechea, F. J.; Frenkel, D. Receptor-Mediated Endocytosis of Nanoparticles of Various Shapes. *Nano Lett.* **2011**, *11*, 5391–5395.

20. Barua, S.; Yoo, J. W.; Kolhar, P.; Wakankar, A.; Gokarn, Y. R.; Mitragotri, S. Particle Shape Enhances Specificity of Antibody-Displaying Nanoparticles. *Proc. Natl. Acad. Sci. U.S.A.* **2013**, *110*, 3270–3275.

21. Harush-Frenkel, O.; Debotton, N.; Benita, S.; Altschuler, Y. Targeting of Nanoparticles to the Clathrin-Mediated Endocytic Pathway. *Biochem. Biophys. Res. Commun.* **2007**, *353*, 26–32.

22. Austin, C. D.; De Mazière, A. M.; Pisacane, P. I.; van Dijk, S. M.; Eigenbrot, C.; Sliwkowski, M. X.; Klumperman, J.; Scheller, R. H. Endocytosis and Sorting of Erbb2 and the Site of Action of Cancer Therapeutics Trastuzumab and Geldanamycin. *Mol. Biol. Cell* **2004**, *15*, 5268–5282.

23. Paulos, C. M.; Reddy, J. A.; Leamon, C. P.; Turk, M. J.; Low, P. S. Ligand Binding and Kinetics of Folate Receptor Recycling *in Vivo*: Impact on Receptor-Mediated Drug Delivery. *Mol. Pharmacol.* **2004**, *66*, 1406–1414.

24. Zhang, L.; Xia, J.; Zhao, Q.; Liu, L.; Zhang, Z. Functional Graphene Oxide as a Nanocarrier for Controlled Loading and Targeted Delivery of Mixed Anticancer Drugs. *Small* **2010**, *6*, 537–544.

25. Sahoo, S. K.; Ma, W.; Labhasetwar, V. Efficacy of Transferrin-Conjugated Paclitaxel-Loaded Nanoparticles in a Murine Model of Prostate Cancer. *Int. J. Cancer* **2004**, *112*, 335–340.

26. Sahoo, S. K.; Labhasetwar, V. Enhanced Antiproliferative Activity of Transferrin-Conjugated Paclitaxel-Loaded Nanoparticles Is Mediated *via* Sustained Intracellular Drug Retention. *Mol. Pharmaceutics* **2005**, *2*, 373–383.

27. Jaxel, C.; Capranico, G.; Kerrigan, D.; Kohn, K. W.; Pommier, Y. Effect of Local DNA Sequence on Topoisomerase I Cleavage in the Presence or Absence of Camptothecin. *J. Biol. Chem.* **1991**, *266*, 20418–20423.

28. Jaxel, C.; Kohn, K. W.; Wani, M. C.; Wall, M. E.; Pommier, Y. Structure–Activity Study of the Actions of Camptothecin Derivatives on Mammalian Topoisomerase I: Evidence for a Specific Receptor Site and a Relation to Antitumor Activity. *Cancer Res.* **1989**, *49*, 1465–1469.

29. Staker, B. L.; Feese, M. D.; Cushman, M.; Pommier, Y.; Zembower, D.; Stewart, L.; Burgin, A. B. Structures of Three Classes of Anticancer Agents Bound to the Human Topoisomerase I–DNA Covalent Complex. *J. Med. Chem.* **2005**, *48*, 2336–2345.

30. Burris, H. A.; Rugo, H. S.; Vukelja, S. J.; Vogel, C. L.; Borson, R. A.; Limentani, S.; Tan-Chiu, E.; Krop, I. E.; Michaelson, R. A.; Girish, S.; *et al.* Phase II Study of the Antibody Drug Conjugate Trastuzumab-Dm1 for the Treatment of Human Epidermal Growth Factor Receptor 2 (Her2)–Positive Breast Cancer after Prior Her2-Directed Therapy. *J. Clin. Oncol.* **2011**, *29*, 398–405.

31. Vogel, C. L.; Cobleigh, M. A.; Tripathy, D.; Gutheil, J. C.; Harris, L. N.; Fehrenbacher, L.; Slamon, D. J.; Murphy, M.; Novotny, W. F.; Burchmore, M.; *et al.* Efficacy and Safety of Trastuzumab as a Single Agent in First-Line Treatment of Her2-Overexpressing Metastatic Breast Cancer. *J. Clin. Oncol.* **2002**, *20*, 719–726.

32. Cobleigh, M. A.; Vogel, C. L.; Tripathy, D.; Robert, N. J.; Scholl, S.; Fehrenbacher, L.; Wolter, J. M.; Paton, V.; Shak, S.; Lieberman, G.; *et al.* Multinational Study of the Efficacy and Safety of Humanized Anti-Her2 Monoclonal Antibody in Women Who Have Her2-Overexpressing Metastatic Breast Cancer That Has Progressed after Chemotherapy for Metastatic Disease. *J. Clin. Oncol.* **1999**, *17*, 2639.

33. Croxtall, J. D.; McKeage, K. Trastuzumab: In Her2-Positive Metastatic Gastric Cancer. *Drugs* **2010**, *70*, 2259–2267.

34. Bang, Y.-J.; Van Cutsem, E.; Feyereislova, A.; Chung, H. C.; Shen, L.; Sawaki, A.; Lordick, F.; Ohtsu, A.; Omuro, Y.; Satoh, T.; *et al.* Trastuzumab in Combination with Chemotherapy *versus* Chemotherapy Alone for Treatment of Her2-Positive Advanced Gastric or Gastro-Oesophageal Junction Cancer (Toga): A Phase 3, Open-Label, Randomised Controlled Trial. *Lancet* **2010**, *376*, 687–697.

35. Slamon, D. J.; Leyland-Jones, B.; Shak, S.; Fuchs, H.; Paton, V.; Bajamonde, A.; Fleming, T.; Eiermann, W.; Wolter, J.; Pegram, M.; *et al.* Use of Chemotherapy Plus a Monoclonal Antibody against Her2 for Metastatic Breast Cancer That Overexpresses Her2. *N. Engl. J. Med.* **2001**, *344*, 783–792.

36. Burstein, H. J.; Harris, L. N.; Gelman, R.; Lester, S. C.; Nunes, R. A.; Kaelin, C. M.; Parker, L. M.; Ellison, L. W.; Kuter, I.; Gadd, M. A.; *et al.* Preoperative Therapy with Trastuzumab and Paclitaxel Followed by Sequential Adjuvant Doxorubicin/Cyclophosphamide for Her2 Overexpressing Stage II or III Breast Cancer: A Pilot Study. *J. Clin. Oncol.* **2003**, *21*, 46–53.

37. Marty, M.; Cognetti, F.; Maraninchi, D.; Snyder, R.; Mauriac, L.; Tubiana-Hulin, M.; Chan, S.; Grimes, D.; Antón, A.; Lluch, A.; *et al.* Randomized Phase II Trial of the Efficacy and Safety of Trastuzumab Combined with Docetaxel in Patients with Human Epidermal Growth Factor Receptor 2 Positive Metastatic Breast Cancer Administered as First-Line Treatment: The M77001 Study Group. *J. Clin. Oncol.* **2005**, *23*, 4265–4274.

38. Jackisch, C. Her-2-Positive Metastatic Breast Cancer: Optimizing Trastuzumab-Based Therapy. *Oncologist* **2006**, *11*, 34–41.

39. Romond, E. H.; Perez, E. A.; Bryant, J.; Suman, V. J.; Geyer, C. E.; Davidson, N. E.; Tan-Chiu, E.; Martino, S.; Paik, S.; Kaufman, P. A.; *et al.* Trastuzumab Plus Adjuvant Chemotherapy for Operable Her2-Positive Breast Cancer. *N. Engl. J. Med.* **2005**, *353*, 1673–1684.

40. Bodley, A.; Liu, L. F.; Israel, M.; Seshadri, R.; Koseki, Y.; Giuliani, F. C.; Kirschenbaum, S.; Silber, R.; Potmesil, M. DNA Topoisomerase II-Mediated Interaction of Doxorubicin and Daunorubicin Congeners with DNA. *Cancer Res.* **1989**, *49*, 5969–5978.

41. Blum, R. H.; Carter, S. K. Adriamycin. *Ann. Intern. Med.* **1974**, *80*, 249–259.

42. Minotti, G.; Menna, P.; Salvatorelli, E.; Cairo, G.; Gianni, L. Anthracyclines: Molecular Advances and Pharmacologic Developments in Antitumor Activity and Cardiotoxicity. *Pharmacol. Rev.* **2004**, *56*, 185–229.

43. Kingsbury, W. D.; Boehm, J. C.; Jakas, D. R.; Holden, K. G.; Hecht, S. M.; Gallagher, G.; Caranfa, M. J.; McCabe, F. L.; Faucette, L. F.; Johnson, R. K.; *et al.* Synthesis of

Water-Soluble (Aminoalkyl)camptothecin Analogs: Inhibition of Topoisomerase I and Antitumor Activity. *J. Med. Chem.* **1991**, *34*, 98–107.

44. Luzzio, M. J.; Besterman, J. M.; Emerson, D. L.; Evans, M. G.; Lackey, K.; Leitner, P. L.; McIntyre, G.; Morton, B.; Myers, P. L.; Peel, M.; *et al.* Synthesis and Antitumor Activity of Novel Water Soluble Derivatives of Camptothecin as Specific Inhibitors of Topoisomerase I. *J. Med. Chem.* **1995**, *38*, 395–401.

45. Nawara, K.; Romiszewski, J.; Kijewska, K.; Szczytko, J.; Twardowski, A.; Mazur, M.; Krysinski, P. Adsorption of Doxorubicin onto Citrate-Stabilized Magnetic Nanoparticles. *J. Phys. Chem. C* **2012**, *116*, 5598–5609.

46. Pommier, Y.; Redon, C.; Rao, V. A.; Seiler, J. A.; Sordet, O.; Takemura, H.; Antony, S.; Meng, L.; Liao, Z.; Kohlhagen, G.; *et al*. Repair of and Checkpoint Response to Topoisomerase I-Mediated DNA Damage. *Mutat. Res., Fundam. Mol. Mech. Mutagen.* **2003**, *532*, 173–203.

47. Chou, T.-C.; Talalay, P. Quantitative Analysis of Dose-Effect Relationships: The Combined Effects of Multiple Drugs or Enzyme Inhibitors. *Adv. Enzyme Regul.* **1984**, *22*, 27–55.

48. Dean-Colomb, W.; Esteva, F. J. Her2-Positive Breast Cancer: Herceptin and Beyond. *Eur. J. Cancer* **2008**, *44*, 2806–2812.

49. Hsiang, Y.-H.; Lihou, M. G.; Liu, L. F. Arrest of Replication Forks by Drug-Stabilized Topoisomerase I-DNA Cleavable Complexes as a Mechanism of Cell Killing by Camptothecin. *Cancer Res.* **1989**, *49*, 5077–5082.

50. Ling, Y. H.; el-Naggar, A. K.; Priebe, W.; Perez-Soler, R. Cell Cycle-Dependent Cytotoxicity, G2/M Phase Arrest, and Disruption of P34cdc2/Cyclin B1 Activity Induced by Doxorubicin in Synchronized P388 Cells. *Mol. Pharmacol.* **1996**, *49*, 832–841.

51. Chen, J.; Irudayaraj, J. Quantitative Investigation of Compartmentalized Dynamics of Erbb2 Targeting Gold Nanorods in Live Cells by Single Molecule Spectroscopy. *ACS Nano* **2009**, *3*, 4071–4079.

52. Colin, J. T.; Anna, C. R.; Krysten, J. P.; Thomas, W.; Jacqueline, O.; Naomi, A.; Jez, G. C.; Joachim, K.; David, J. S.; Peter, J. C. Snx4 Coordinates Endosomal Sorting of Tfnr with Dynein-Mediated Transport into the Endocytic Recycling Compartment. *Nat. Cell Biol.* **2007**, *9*, 1370–1380.

53. Humblet, V.; Misra, P.; Bhushan, K. R.; Nasr, K.; Ko, Y.-S.; Tsukamoto, T.; Pannier, N.; Frangioni, J. V.; Maison, W. Multivalent Scaffolds for Affinity Maturation of Small Molecule Cell Surface Binders and Their Application to Prostate Tumor Targeting. *J. Med. Chem.* **2009**, *52*, 544–550.

54. Decuzzi, P.; Ferrari, M. The Adhesive Strength of Non-spherical Particles Mediated by Specific Interactions. *Biomaterials* **2006**, *27*, 5307–5314.

55. Decuzzi, P.; Ferrari, M. The Receptor-Mediated Endocytosis of Nonspherical Particles. *Biophys. J.* **2008**, *94*, 3790–3797.

56. Muro, S.; Garnacho, C.; Champion, J. A.; Leferovich, J.; Gajewski, C.; Schuchman, E. H.; Mitragotri, S.; Muzykantov, V. R. Control of Endothelial Targeting and Intracellular Delivery of Therapeutic Enzymes by Modulating the Size and Shape of Icam-1-Targeted Carriers. *Mol. Ther.* **2008**, *16*, 1450–1458.

57. Jin, H.; Heller, D. A.; Sharma, R.; Strano, M. S. Size-Dependent Cellular Uptake and Expulsion of Single-Walled Carbon Nanotubes: Single Particle Tracking and a Generic Uptake Model for Nanoparticles. *ACS Nano* **2009**, *3*, 149–158.

58. Park, J.-H.; von Maltzan, G.; Zhang, L.; Derfus, A. M.; Simberg, D.; Harris, T. J.; Ruoslahti, E.; Bhatia, S. N.; Sailor, M. J. Systematic Surface Engineering of Magnetic Nano-worms for *In Vivo* Tumor Targeting. *Small* **2009**, *5*, 694–700.

59. Huang, X.; Teng, X.; Chen, D.; Tang, F.; He, J. The Effect of the Shape of Mesoporous Silica Nanoparticles on Cellular Uptake and Cell Function. *Biomaterials* **2010**, *31*, 438–448.

60. Kolhar, P.; Mitragotri, S. Polymer Microparticles Exhibit Size and Shape Dependent Accumulation around the Nucleus after Endocytosis. *Adv. Funct. Mater.* **2012**, *22*, 3759–3764.

61. Xu, Z. P.; Niebert, M.; Porazik, K.; Walker, T. L.; Cooper, H. M.; Middelberg, A. P. J.; Gray, P. P.; Bartlett, P. F.; Lu, G. Q. Subcellular Compartment Targeting of Layered Double Hydroxide Nanoparticles. *J. Controlled Release* **2008**, *130*, 86–94.

62. Croce, A. C.; Bottiroli, G.; Supino, R.; Favini, E.; Zuco, V.; Zunino, F. Subcellular Localization of the Camptothecin Analogues, Topotecan and Gimatecan. *Biochem. Pharmacol.* **2004**, *67*, 1035–1045.

63. Poon, I. K. H.; Jans, D. A. Regulation of Nuclear Transport: Central Role in Development and Transformation? *Traffic* **2005**, *6*, 173–186.

64. Misra, R.; Sahoo, S. K. Intracellular Trafficking of Nuclear Localization Signal Conjugated Nanoparticles for Cancer Therapy. *Eur. J. Pharm. Sci.* **2010**, *39*, 152–163.

65. Yu, J.; Xie, X.; Zheng, M.; Yu, L.; Zhang, L.; Zhao, J.; Jiang, D.; Che, X. Fabrication and Characterization of Nuclear Localization Signal-Conjugated Glycol Chitosan Micelles for Improving the Nuclear Delivery of Doxorubicin. *Int. J. Nanomed.* **2012**, *7*, 5079–5090.

66. Gillies, E. R.; Fréchet, J. M. J. pH-Responsive Copolymer Assemblies for Controlled Release of Doxorubicin. *Bioconjugate Chem.* **2005**, *16*, 361–368.

67. Dong, D.-W.; Tong, S.-W.; Qi, X.-R. Comparative Studies of Polyethylenimine−Doxorubicin Conjugates with pH-Sensitive and pH-Insensitive Linkers. *J. Biomed. Mater. Res., Part A* **2013**, *101A*, 1336–1344.

68. Dalmark, M.; Johansen, P. Molecular Association between Doxorubicin (Adriamycin) and DNA-Derived Bases, Nucleosides, Nucleotides, Other Aromatic Compounds, and Proteins in Aqueous Solution. *Mol. Pharmacol.* **1982**, *22*, 158–165.

69. Mohan, P.; Rapoport, N. Doxorubicin as a Molecular Nano-theranostic Agent: Effect of Doxorubicin Encapsulation in Micelles or Nanoemulsions on the Ultrasound-Mediated Intracellular Delivery and Nuclear Trafficking. *Mol. Pharmaceutics* **2010**, *7*, 1959–1973.

70. Robert, J.; Illiadis, A.; Hoerni, B.; Cano, J.-P.; Durand, M.; Lagarde, C. Pharmacokinetics of Adriamycin in Patients with Breast Cancer: Correlation between Pharmacokinetic Parameters and Clinical Short-Term Response. *Eur. J. Cancer Clin. Oncol.* **1982**, *18*, 739–745.

71. Potter, A. J.; Gollahon, K. A.; Palanca, B. J. A.; Harbert, M. J.; Choi, Y. M.; Moskovitz, A. H.; Potter, J. D.; Rabinovitch, P. S. Flow Cytometric Analysis of the Cell Cycle Phase Specificity of DNA Damage Induced by Radiation, Hydrogen Peroxide and Doxorubicin. *Carcinogenesis* **2002**, *23*, 389–401.

72. Wall, M. E.; Wani, M. C.; Cook, C. E.; Palmer, K. H.; McPhail, A. T.; Sim, G. A. Plant Antitumor Agents. I. The Isolation and Structure of Camptothecin, a Novel Alkaloidal Leukemia and Tumor Inhibitor from Camptotheca Acuminata1,2. *J. Am. Chem. Soc.* **1966**, *88*, 3888–3890.

73. Junttila, T. T.; Akita, R. W.; Parsons, K.; Fields, C.; Lewis Phillips, G. D.; Friedman, L. S.; Sampath, D.; Sliwkowski, M. X. Ligand-Independent Her2/Her3/Pi3k Complex Is Disrupted by Trastuzumab and Is Effectively Inhibited by the Pi3k Inhibitor Gdc-0941. *Cancer Cell* **2009**, *15*, 429–440.

74. Laginha, K. M.; Verwoert, S.; Charrois, G. J. R.; Allen, T. M. Determination of Doxorubicin Levels in Whole Tumor and Tumor Nuclei in Murine Breast Cancer Tumors. *Clin. Cancer Res.* **2005**, *11*, 6944–6949.

75. De Jong, W. H.; Hagens, W. I.; Krystek, P.; Burger, M. C.; Sips, A. J. A. M.; Geertsma, R. E. Particle Size-Dependent Organ Distribution of Gold Nanoparticles after Intravenous Administration. *Biomaterials* **2008**, *29*, 1912–1919.

76. Wiegand, S.; Heinen, T.; Ramaswamy, A.; Sesterhenn, A. M.; Bergemann, C.; Werner, J. A.; Lübbe, A. S. Evaluation of the Tolerance and Distribution of Intravenously Applied Ferrofluid Particles of 250 and 500 nm Size in an Animal Model. *J. Drug Targeting* **2009**, *17*, 194–199.

77. Hyung Park, J.; Kwon, S.; Lee, M.; Chung, H.; Kim, J.-H.; Kim, Y.-S.; Park, R.-W.; Kim, I.-S.; Bong Seo, S.; Kwon, I. C.; *et al*. Self-Assembled Nanoparticles Based on Glycol Chitosan Bearing Hydrophobic Moieties as Carriers for Doxorubicin: *In Vivo* Biodistribution and Anti-tumor Activity. *Biomaterials* **2006**, *27*, 119–126.

78. Yuan, F.; Dellian, M.; Fukumura, D.; Leunig, M.; Berk, D. A.; Torchilin, V. P.; Jain, R. K. Vascular Permeability in a Human Tumor Xenograft: Molecular Size Dependence and Cutoff Size. *Cancer Res.* **1995**, *55*, 3752–3756.

79. Kolhar, P.; Anselmo, A. C.; Gupta, V.; Pant, K.; Prabhakarpandian, B.; Ruoslahti, E.; Mitragotri, S. Using Shape Effects To Target Antibody-Coated Nanoparticles to Lung and Brain Endothelium. *Proc. Natl. Acad. Sci. U.S.A.* **2013**, *110*, 10753–10758.